Coupled molecular dynamics-Monte Carlo model to study the role of chemical processes during laser ablation of polymeric materials

Manish Prasad, Patrick F. Conforti, and Barbara J. Garrison[a)]
Department of Chemistry, 104 Chemistry Building, The Pennsylvania State University, University Park, Pennsylvania 16802, USA

(Received 17 April 2007; accepted 6 June 2007; published online 24 August 2007)

The coarse grained chemical reaction model is enhanced to build a molecular dynamics (MD) simulation framework with an embedded Monte Carlo (MC) based reaction scheme. The MC scheme utilizes predetermined reaction chemistry, energetics, and rate kinetics of materials to incorporate chemical reactions occurring in a substrate into the MD simulation. The kinetics information is utilized to set the probabilities for the types of reactions to perform based on radical survival times and reaction rates. Implementing a reaction involves changing the reactants species types which alters their interaction potentials and thus produces the required energy change. We discuss the application of this method to study the initiation of ultraviolet laser ablation in poly(methyl methacrylate). The use of this scheme enables the modeling of all possible photoexcitation pathways in the polymer. It also permits a direct study of the role of thermal, mechanical, and chemical processes that can set off ablation. We demonstrate that the role of laser induced heating, thermomechanical stresses, pressure wave formation and relaxation, and thermochemical decomposition of the polymer substrate can be investigated directly by suitably choosing the potential energy and chemical reaction energy landscape. The results highlight the usefulness of such a modeling approach by showing that various processes in polymer ablation are intricately linked leading to the transformation of the substrate and its ejection. The method, in principle, can be utilized to study systems where chemical reactions are expected to play a dominant role or interact strongly with other physical processes. © *2007 American Institute of Physics*. [DOI: 10.1063/1.2754681]

I. INTRODUCTION

Laser ablation occurs in a diverse range of materials from molecular solids, biological tissues, crystalline metals, and semiconductors to polymeric materials. The laser ablation process parameters can also be selected from a large set, ranging from short ultraviolet (UV) to long infrared (IR) wavelengths, from short femtosecond to long microsecond pulse widths, and from low pulse energy in kilowatts up to as high as several gigawatts.[1] The response to laser irradiation depends directly on the material characteristics and the laser process parameters along with spot size and repetition rate.[2–15] Typically, laser irradiation of a material causes electronic excitation, possibly followed by substrate heating, bond cleavage, desorption, chemical reactions, thermal decomposition, melting, propagation of stress waves, mechanical failure, and/or bulk ejection of material. The laser ablation process is of technological interest with applications ranging from chemical analysis, medical diagnostics and treatment, micromachining to fabrication of electronic, optoelectronic devices, and nanomaterials.[12,14–17] A detailed mechanistic insight into the role of material properties and the process parameters in initiating laser ablation is necessary so as to further optimize and develop these applications.

An array of experimental work has been done to observe the multitude of processes occurring upon laser irradiation of polymeric substrates and develop an understanding of the mechanisms leading to ablation. Photon absorption spectrum and penetration depth measurements have been reported for many useful polymer substrates.[18–20] Wen and Dlott have used optical calorimetry to measure substrate temperature change by exciting a near-IR dye embedded in the polymer and deduced a two stage heating and vibrational excitation process.[21] Photoacoustic measurements have given peak stress generated as a function of fluence in a poly (methyl methacrylate) (PMMA) substrate[22] and picosecond coherent anti-Stokes Raman spectroscopy was used to measure dynamic frequency shift in the PMMA substrate to infer rise in substrate temperature, volume expansion, critical stress at ablation threshold, and establish buildup of compressive pressure in the substrate due to thermal loading and chemical transformation.[23] Analytical techniques such as gel permeation chromatography, UV spectroscopy, x-ray photoelectron spectroscopy, nuclear magnetic resonance, and Fourier transform IR have been used to identify radicals and chemical reaction products and measure quantum yield and substrate transformation pathways (e.g., incubation) occurring upon photolysis.[11,18,20,24,25] Stress wave propagation, bubble formation, and spallation in some substrates upon laser excitation have also been confirmed.[10,26] Experiments reporting surface swelling, melting, thermal damage, and measurements of ablation/etch rates as a function of laser

[a)]Author to whom correspondence should be addressed. Electronic mail: bjg@psu.edu

processing parameters provide a direct way of judging the suitability of a polymer for a given application.[3,14,17,27,28] The ejected plume has been characterized using a combination of gas chromatography, time of flight measurement, and mass spectrometry (MS) to identify plume composition and to infer possible photoexcitation pathways and ablation mechanisms.[2,5–7,9,18,29] MS measurements of velocities of molecular fragments ejected upon laser irradiation have shown thermal Maxwell-Boltzmann and/or nonthermal velocity distribution, indirectly addressing the nature and mechanism of their ejection.[30] The effects of dopant concentration, molecular weight, and chain length on the onset of ablation have also been studied in doped and undoped polymer substrates to examine the role of polymer properties in establishing ablation.[8,9,28,31,32] However, even with this wealth of experimental data available, a complete and coherent picture of how ablation is established in a polymeric substrate is yet to emerge.

The experimental work has been complemented by theoretical and modeling efforts. Earliest models proposed Beer's law based dependence of the ablated yield on fluence following a complete photothermal and/or photochemical destruction of polymer chains.[33] Processing parameters, such as pulse width and repetition rates, were incorporated by suggesting that a certain threshold concentration of absorbed photons is required for photoexcitation to lead to ablation.[34] Excited electronic states and chemical reactions were incorporated with the aim to model substrate modification by chemical and thermal pathways.[35,36] The role of mechanical strength of substrate as well as laser induced stress generation, void nucleation, void formation, and spallation in initiating ablation has also been studied.[37,38] More recently, pure thermal ablation models are built taking into consideration thermally activated bond breaks, creation of small molecules in the bulk, and surface desorption. These processes cause reduction in the cohesive energy of the polymer and removal of material when the number of broken bonds exceeds a critical value.[36,39] Likewise, recent photochemical models incorporate the change in the characteristics of the substrate due to multiple photochemical modification pathways.[36,40] The ablation models have played a great role in developing an understanding of the process and material parameters, but most of them are still largely based on a phenomenological picture and often lack microscopic insights into the ablation process.[41]

Atomistic scale studies can serve as a bridge between the experimental and numerical modeling approaches by providing direct insight into the microscopic processes responsible for the experimental observables. These insights can be used to build better physical process models. The ablation process dynamics is complex involving many possible thermal, mechanical, and chemical processes. In addition, these processes can lead to simultaneous modification of physiochemical properties of the substrate during laser irradiation. The advantage of molecular dynamics (MD) based modeling is that a qualitatively realistic and physical representation of most of these processes can be provided with minimal representation, i.e., by defining the potential and reaction energy landscapes. For example, the effect of mechanical stresses generated by high temperature and creation of volatile species, which can alter reaction and activation energies governing thermal and chemical processes, and cause ablation via mechanical failure, is included naturally in a MD model. Other effects, such as variation of physical properties of polymer substrates with changing composition and screening of laser radiation by the ablating plume, that are not as simple or straightforward to be described accurately in a numerical model, can be incorporated in a MD simulation to study their role in setting ablation.

The earliest MD studies suggested that stress buildup and volume expansion in the substrate, caused by formation of smaller molecules, play a key role in the subsequent ejection of material.[42] Rates of vibrational energy transfer in molecular clusters have been measured using MD simulations.[43] A breathing sphere model was used to model electronic excitation and ionization processes in atoms and molecules, where an internal breathing mode was used to describe photon absorption, internal conversion, and vibrational relaxation processes in these species.[44,45] This model has been used extensively to study dependence of ablation pathways on laser processing parameters such as fluence, pulse width, and also the role of mechanical stresses.[46] Furthermore, the breathing sphere model has been extended to incorporate photofragmentation pathways in MD simulation and study the role of chemical reactions in substrate modification and on plume composition.[47–49] Electronic structure calculations have also been performed to determine photodegradation reaction pathways and energies for materials constituting the substrates.[50–52] This information has been used to build a more physically representative coarse grain chemical reaction model (CGCRM) for polymer ablation.[53,54] In another interesting set of MD studies reported recently, ablation processes in idealized Lennard-Jones and pure one component metallic and silicon substrates have been analyzed using phase diagrams based on local thermal equilibrium argument.[55] Such analyses, however, would be near impossible to perform on multicomponent and polymeric systems that can decompose upon laser excitation.

In this article, we describe an extension of the original CGCRM model[53,54] for studying ablation of polymeric materials. As discussed above, most of the earlier studies have not looked into the effect of chemical reactions on these substrates after laser irradiation. The purpose of building this model is to create an *integrated* setup to explore various thermal, mechanical, and chemical processes that may be responsible for initiating ablation. Using PMMA as a model polymeric substrate, we discuss in Sec. II the construction and parametrization of the polymer-MD system. The chemical reactions, in the PMMA substrate, arise out of the photofragmentation, radical formation, and thermal decomposition processes. These reactions are included based on a Monte Carlo (MC) scheme embedded within the MD simulation framework. The algorithm for incorporating these reactions is described in Sec. III. The key issues related to the ablation process in the PMMA substrate are discussed in brief in Sec. IV, followed by the application of our modeling strategy to the study of laser ablation in PMMA.

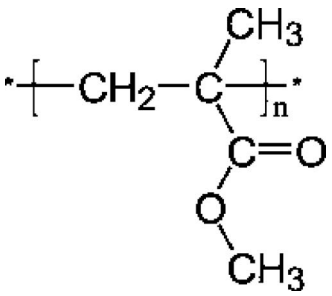

FIG. 1. Monomeric unit of the PMMA polymer is shown here. Each atom or group of atoms represents a coarse grained bead in the simulation. Norrish type I corresponds to break in C–CO bond, whereas Norrish type II is a break in CH_2–C bond.

II. COARSE GRAINED POLYMER-MD MODEL

A. Polymer coarse graining

The polymeric substrates for ablation modeling are built using a coarse grained united atom representation. Each polymer chain was made up of a set of coarse grained "beads" or superatoms each representing a functional group.[54] This coarse graining permits the use of larger system sizes and longer simulation time scales compared to purely atomic systems by reducing the number of atoms to simulate and eliminating fast C–H and unnecessary and computationally expensive C═O interactions. For PMMA, our model polymer, these functional groups are CH_x $(0 \leqslant x \leqslant 3)$, C═O and O, as shown in Fig. 1. Various other functional groups involved in the simulation, e.g., due to creation of radicals ($\bullet CH_3$) and reaction products (HCO, CH_4, and OH), are also part of the set of species. Each coarse grained bead or superatom is identified by a separate species type. The bonding and angular potentials are based on the species type as well as the organization of the bonding network in the polymer chain which is specific to the polymer and added as an input in our MD model. Here, the exact matching of fully atomistic equilibrium distribution of bond lengths and angles is not vital for coarse graining as ablation simulation will be sampling states far from equilibrium.

B. Potential energy model

The bonding potentials between any two functional groups are of the harmonic form, i.e., $U_{\text{bond}}=K_{\text{bond}}(r-r_0)^2$, where r is the instantaneous bond length and r_0 the equilibrium bond length. These potentials are taken directly from the atomistic scale model by Kim *et al.*[56] The equilibrium radii and bond lengths of the coarse grained beads have been computed earlier.[54] Ablation simulations, however, can reach states far from equilibrium involving high temperatures and pressures. These thermodynamic conditions can lead to bond breaks under realistic conditions. To accommodate these "thermally or stress induced" bond breaks, all bonding potentials (except those for double bonds) are switched to Morse potentials of the form

$$U_{\text{bond}} = A[1 - \exp(-B(r - r_0))]^2 + C, \tag{1}$$

for bond lengths greater than 3% of equilibrium bond length.[54,57] Morse potential parameters, A, B, and C, are fitted individually to each bonding potential to ensure continuity in potential energy and forces. The use of this hybrid potential allows us to turn off the Morse interaction for high temperature annealing simulations during preparation of polymer samples.

The angular potentials are of pure harmonic form and are also taken directly from Kim *et al.*[56] To prevent a sudden transition from finite angular potential to zero potential due to bond breaks a screening function of the form, $\exp(-2(r-r_c)^2)$, is employed beyond a cutoff value of r_c for each of the two bonds forming a bond angle. The general expression for angular potential energy function is given by

$$U_\theta = K_\theta(\theta - \theta_0)^2 \exp(-2(r^{ab} - r_c^{ab})^2)\exp(-2(r^{bc} - r_c^{bc})^2), \tag{2}$$

where θ is the angle formed at atom b between atom pairs a-b and b-c, whose instantaneous interaction distance is given by r^{ab} and r^{bc}, and cutoff interaction distances given by r_c^{ab} and r_c^{bc}, respectively. The value θ_0 is the equilibrium value of the bond angle θ. The cutoff distance was set larger than the equilibrium bond length and a value of 3 Å was employed for all angular potentials. Four-body torsional interactions were not included as they are not considered important for the ablation dynamics.[54]

The nonbonding inter- and intramolecular interactions are described using another Morse potential fitted to match PMMA physical properties such as the cohesive energy[58] and glass transition temperature.[59] The parameters for the nonbonded interactions were independent of the types of species interacting and set at $A=0.042$ eV, $B=1.025$ Å^{-1}, $C=-A$, $r_0=4.35$ Å for the PMMA sample. Additional Morse type potential energy functions characterizing nonbonded interactions between two radicals, and a radical and a nonradical are defined to match the appropriate reaction energy change occurring during bond breaks.[47] Bonded interactions among radicals and nonradicals are treated as those among nonradicals of similar species types, i.e., a CH_3 radical is treated as a CH_3 bead for all its bonding and angular interactions. The cutoff distance for all bonding, angular, and nonbonding interaction was set at 10 Å and the Verlet neighbor list cutoff was set at 12 Å.

C. Sample preparation

The sample was prepared by starting with a low density polymer built by random insertion. The first bead of a polymer chain is placed at a low density site followed by addition of the next bead along a random vector at a bond length distributed about its equilibrium value. This step is followed by insertion of more beads, one monomer unit at a time, based on the distribution of bond lengths and angles until the entire polymer chain is built. If any added bead is found too close to any bead on existing polymer chains, it is discarded and a new position is tried. If there is an overlap after multiple attempts, the chain construction is traced backwards and continued from an earlier point. The individual polymer chains were built in a periodic box of fixed size, sequentially using the united atom description, until the total density reached about 0.7–0.8 gm/cm^3.

The prepared sample was then subjected to a series of energy minimization, constant temperature and volume (*NVT*) MD, and compression steps. This process is carried out according to the method described in Refs. 60–62. Only the purely repulsive part of the nonbonded interaction was turned on during these cycles to avoid any clustering in the system due to the attractive part of the potential.[60,61] The bonding potentials were set to be purely harmonic, i.e., the weakening of the bonding potential with the Morse term described above in Eq. (1) was turned off during these cycles, to avoid any fragmentation in the polymer matrix prior to laser excitation. Each stage involved 10 000 steps of energy minimization, followed by 20 000 time steps of *NVT* run at 600 K corresponding to 20 ps of simulation time. The high temperature *NVT* dynamics help the system escape from intermediate local minima.[62] At the end of each *NVT* run the sample was compressed by scaling each of *xyz* dimensions by a factor of 0.99 and sent to quench cycle of the next stage. This series of runs was carried out until the sample density reached above the bulk polymer density to a value in the range of 1.20–1.25 gm/cm^3, which is one compression stage beyond the desired bulk density (1.20 gm/cm^3). The sample is initially compressed beyond its desired bulk density to incorporate any pressure induced relaxation.[60] The high density sample is then relaxed back to the correct density. Next, the correct long-ranged nonbonding potentials are introduced into the polymer sample. This process is carried out in four stages, each stage with 10 000 steps of energy minimization followed by 20 000 time steps of *NVT*-MD. During each of energy minimization stage, a quarter of the attractive part of the interaction potential is turned on. Following this step, the sample is subjected to additional 200 000–400 000 time steps of *NVT*-MD simulation at 300 K, with the weakening of bonds [Eq. (1)] turned on and periodic boundary condition removed from *z* axis, to fully equilibrate the substrate, i.e., to relax it to its zero pressure and lowest energy state.

D. Boundary conditions for ablation

During an ablation simulation, periodic boundary conditions are applied to the sides (*xy* axes) and a pressure absorbing boundary condition (PABC) is applied at the bottom of the sample to prevent the downward traveling pressure wave from reflecting back into the sample.[63] These boundary conditions together mimic a deep substrate (i.e., no reflected pressure wave is formed at the back end of the sample at all times) at the center of laser pulse where the mass and energy transfers are expected only along the depth of the sample. For the implementation of the PABC, the bottom part of the sample, equal to the length used for the Verlet list construction, is selected as the pressure absorbing boundary layer. The force, along the *z* axis, acting on any particle in the boundary layer is divided into two parts—those acting due to particles above it (i.e., higher up in *z* axis) and those acting due to particles below it. The forces due to particles below it are then replaced by terminating forces, which replicate an infinite continuum below the finite-sized sample. The termination forces have three components—F_0, the static equilibrium forces, which balances out the forces from top part of the sample; F_L, the forces generated due to direct laser energy absorption by the boundary region; and F_W, the forces due to the propagation of a pressure wave through the boundary region. The last two terms can be written as[63]

$$F_L = \frac{A\Gamma\Phi}{L_P}\exp\left(-\frac{z_b}{L_P}\right) \quad \text{for } t \leqslant \tau$$

and

$$F_L = \frac{A\Gamma\Phi}{L_P}\exp\left(-\frac{z_b}{L_P}\right)\left[\frac{L_P}{tc}\times\left(1-\exp\left(\frac{tc}{L_P}\right)\right)\right] \quad \text{for } t > \tau, \tag{3}$$

$$F_W = S_M Z u, \tag{4}$$

where A is the area illuminated by the laser, Γ is the Grüneisen coefficient, Φ is the laser fluence, z_b is the average depth of the boundary layer, L_P is the penetration depth of the sample, t is the time of irradiation, and τ is the laser pulse width. Also, S_M represents the surface area per particle, u is the average particle velocity in the boundary layer, and $Z = \rho c$ is the acoustic impedance corresponding to density ρ and the sound velocity in the medium c. For F_L, the above Eq. (3) represent forces linearly increasing with time due to laser absorption during irradiation followed by a gradual damping given by the term in square brackets in the second expression. Likewise for F_W, the force corresponds to a one dimensional pressure wave traveling with speed of sound c and local particle velocity u.[63,64]

The determination of the parameters required for the PABC was performed in a separate set of simulations. To compute F_0 and F_L, equilibrium simulations were performed at 200–700 K and over the densities of 1.14–1.30 gm/cm^3. For evaluation purpose, the static equilibrium forces were further resolved in two long-ranged components, inter- and intramolecular nonbonded forces. The static forces coming from the bonding and angular interactions were taken as is, i.e., based on instantaneous distances and angles, evaluated directly in ablation simulations and not evaluated in these equilibrium simulations. The equilibrium simulations were performed on equilibrated PMMA substrates—(a) 3723 beads, with 51 polymer chains each made up of 13 monomeric units, in a sample of size 45 Å^3, and (b) 29785 beads, with 259 polymers each of chain length of 19 units, in a sample of size $51\times51\times258$ Å^3. The middle third part of the sample (b) was used to compute distribution of forces along the *z* axis acting on particles from the particles present below it over a time period of 200 ps. The resulting distribution at 300 K and 1.20 gm/cm^3 is shown in Fig. 2. The most probable values obtained from the distribution were used in the ablation simulation reported in this article. Equilibrium simulations were also used for evaluation of the Grüneisen coefficient which is defined as internal energy derivative of pressure at constant volume,[65]

$$\Gamma = v\left(\frac{dP}{dE}\right)_v, \tag{5}$$

where v is the specific volume, P the pressure, and E the internal energy. For evaluating the derivative, the ensemble

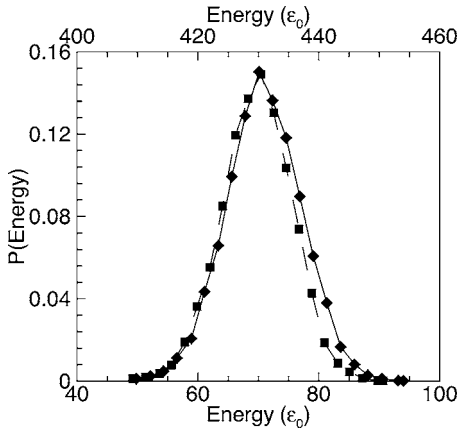

FIG. 2. Distribution of the nonbonding interaction energies among PMMA beads at a density of 1.2 gm/cm^3 and 300 K, computed using sample (b). The dashed curve (squares on the bottom x axis corresponds to the intermolecular interations while the solid curve atoms (diamonds) on the tip x axis is for the intramolecular interactions. Both the energy scales correspond to eV.

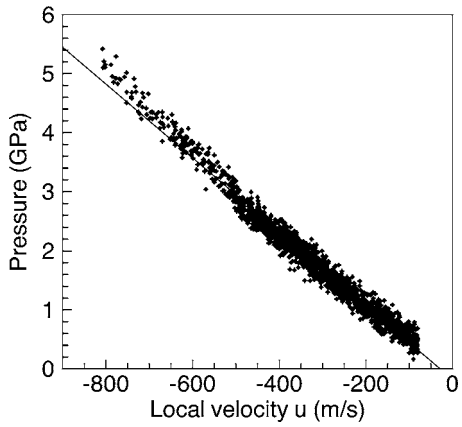

FIG. 4. Pressure vs local velocity computed from impulse simulations. The data shown correspond to a constant downward impulsive force of 1 eV/Å applied over 100 fs in the largest sample (c). The data are collected over 10 ps time scale, from the time of formation of the pressure wave near the top surface to just before it interacts with the bottom surface. Only points used for data fitting are shown.

averages of pressure and internal energy are recorded at every density and temperature over 200 ps of *NVT* runs. The resulting plot of Grüneisen coefficient as a function of density is shown in Fig. 3 and is in good agreement with the reported values.[65,66] The value of 0.60 was used for the ablation simulations reported here. The ablation simulation parameters were chosen so that the sample temperature at the bottom does not increase significantly above 300 K, thus justifying the use of these values for computation of F_0 and F_L.

The acoustic impedance parameter Z was evaluated by performing nonequilibrium simulations without z periodicity. These simulations were done using sample (b) specified above and a larger sample (c) 109 365 beads, with 951 polymer chains of 19 chain length each in system of size $51 \times 51 \times 936$ Å^3, both equilibrated at 300 K. In each simulation, a downward impulsive force in the range of 1–10 eV/Å is imparted onto the top 10 Å layer of the sample over a period of 10–100 fs (10–100 steps). The application of the impulse is similar to the ultrafast laser heating and shock compression experiments and results in the impulse energy being transformed into a pressure wave which propagates into the substrate.[67] The evolution of the

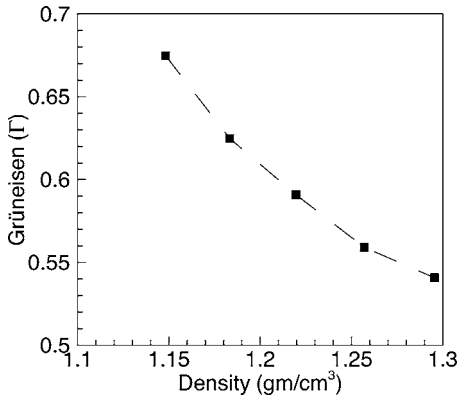

FIG. 3. Grüneisen coefficient Γ, computed as a function of density (in gm/cm^3), from simulations using sample (a), performed over a temperature range of 200–600 K. The dashed curve is added as a guide.

substrate is followed by dividing the sample into 10 Å slices and computing its pressure, z forces, and z velocities as a function of depth and time. The plot of local z velocities and pressure following a downward impulsive force of 1 eV/Å over 100 fs is shown in Fig. 4. The data points on the plot correspond to sometime after the pressure wave is formed at the top surface to the time just before it starts interacting with the bottom surface, which is set as a free boundary. The slope of the linear fit gives the acoustic impedance parameter $Z=(4.3-7.3)\times 10^6$ N s/m^3, using $P=-Zu$, over all the impulse runs. The value of acoustic impedance is somewhat higher than the expected value ($\sim 3\times 10^6$ N s/m^3),[68] but well within the range reported in experimental studies.[67] The linear fit in Fig. 4 appears to deviate from the simulation data points for highest pressures and local velocities suggesting a nonlinear relationship. Also, the xy periodic lattice prevents any lateral relaxation, so this system is unlike any real system, which may contribute to the deviation. The mean value obtained over these simulations $\sim 6\times 10^6$ N s/m^3 was used in the ablation simulations reported here.

In the implementation of the PABC, all the xy component of forces and velocities are zeroed out for beads lying in the boundary layer. Also, all the forces along the z direction are averaged and applied equally to all the beads in the pressure absorbing boundary layer to make the PABC provide a rigid piston for efficient pressure transmission. This procedure includes averaging over the bonding and angular forces as well.

III. MODELING LASER-POLYMER INTERACTION

A. Photon absorption process

A laser pulse of wavelength (λ) pulse width (τ), and penetration depth ($1/\alpha$) was applied to all the samples from $t=0$ to $t=\tau$ in the ablation studies reported here. The photons are absorbed by the chromophores (–C– or –CO– in the case of PMMA) in accordance with Beer's law. Suitable laser fluences were identified based on two criteria—the fraction of chromophores absorbing photons should be less than

100% in the top surface layer to prevent chromophore saturation and the fraction of chromophores absorbing photons at the bottom layer should approach zero, i.e., being small in the range of 1%–5%. The beads in the boundary layer subject to the PABC do not directly absorb any photons. These conditions along with Beer's law set the distribution profile of photons and energy absorption in the substrate. Beer's law based absorption profile mimics the entire absorption volume as a scaled down version of a real sample undergoing ablation process, as opposed to uniform absorption profile, which only models surface absorption and ablation processes.

The absorbed photon energy can be directed into one of the many proposed paths—vibrational excitation of the chromophores, direct heating the polymer substrate, and direct bond break and radical formation. The vibrational excitation can be effected by changing the radius of the chromophore or imparting the kinetic energy to its internal mode as done in the breathing sphere models.[44,53] Direct heating is implemented by distributing the photon energy over a monomeric unit (six beads for PMMA as shown in Fig. 1) corresponding to absorption as kinetic energy. Direct photochemical bond break and radical formation is achieved by randomly breaking a bond between the absorbing chromophore and one of its neighbors. The species involved in the bond break are assigned new radical species types and their interaction changes from bonding and angular to nonbonding. The radicals are tagged and their time of existence is recorded for subsequent reactions. In addition to direct bond breaks, heating or stress induced bond breaks are also possible as mentioned above for all cases. Following the thermomechanical bond breaks, however, the coarse grained beads are not labeled as radicals in the simulation scheme and no subsequent reaction occurs.

Formation of radicals in the substrate leads to chemical reactions which can play an important role in ablation.[2,9,29,30,69] There are a vast number of possible reactions that can take place during ablation given the high temperatures, stresses, and types of radicals prevailing in the substrate. The selection of chemical reactions to form the basis set in our MC based reaction scheme is therefore crucial to the development of a feasible and realistic MD simulation scheme. Inclusion of too many reactions can easily slow down our MD time integration without adding any significant new physics to the ablation process. This selection process also relies upon the choice of material to be ablated and is therefore discussed in the next section with reference to our model material PMMA. The purpose of the MD simulation is not to suggest what chemical reaction takes place but to predict how these reactions affect the substrate and the ablation process.

B. Modeling chemical reactions

The reaction scheme used to perform reactions is based on a modified version of the CGCRM.[53,54] All the reaction pathways, Arrhenius reaction rates, and formation energies used in the scheme are *predetermined*. These quantities can be obtained from standard chemistry and chemical engineering (experimental or theoretical) databases,[48] computed using first principles studies[52] or using exotic MD schemes such as reactive-MD.[51] At each step radicals attempt to react with other species present in their vicinity. The MD simulation along with the embedded MC reaction scheme is shown in Fig. 5. For any radical, the chemical reaction algorithm can be described as follows.

(a) All possible reacting species $\{i\}$ are identified within an interaction radius of 2 Å.

(b) If two radicals are next to each other the corresponding radical-radical recombination reaction is selected and tried [step (e)]. Else, the reaction rates k_{riX} of the radical r reacting with other species i is calculated based on individual reaction type X, using their activation energy (E_{AX}), the local temperature (T_L), and the Arrhenius reaction rate expression:[54] $k_{riX}=10^{13}\exp(-E_{AX}/k_BT_L)\ \mathrm{s}^{-1}$, where k_B is the Boltzmann constant.

(c) The total forward reaction rate k_{rT} is computed by summing over all possible reaction rates, i.e., $k_{rT}=\Sigma_i k_{riX}$. The radical survival probability $p(t_r)$ at that step is then computed based on the radical existence time t_r and the total reaction rate using[70] $p(t_r)=\exp(-k_{rT}t_r)$. A random number ξ is then drawn and reaction is attempted if $\xi > p(t_r)$.

(d) Another random number ζ selects the type of reaction to attempt based on the relative weights of each reaction type k_{riX}/k_{rT}, i.e., reaction of type X with between species r and η is selected if $\Sigma_{i=1}^{\eta-1}k_{riX}/k_{rT} < \zeta < \Sigma_{i=1}^{\eta}k_{riX}/k_{rT}$.

(e) The selected reaction is tried by changing the species types of the reacting beads, which changes the interactions between reacting beads and their neighbors. The trial process assesses the feasibility of the selected reaction by measuring the energy difference between the reactant and product states, $\varepsilon_r=\varepsilon_{\mathrm{product}}-\varepsilon_{\mathrm{reactant}}$. The decision to accept the reaction is based on the following scheme.

  (i) If the energy ε_r is within 10% of the desired chemical reaction energy ε_r^d, or 0.1 eV, depending on which ever is higher, the trial is accepted. Note that the desired chemical reaction energy depends only on the reaction type X.

  (ii) Else, if the absolute value of the difference $|\varepsilon_r-\varepsilon_r^d|$ is greater than 2.5 eV then the reaction is abandoned and the species are reverted back to their original states and MD simulation continued.

  (iii) Else, if the reaction energy is within 2.5 eV of the desired value, a steepest descent based optimization of the reactant state is attempted. The aim is to reorganize the local volume around the radicals, i.e., rearrange the participating radicals and their interacting neighbors to obtain a new set of reactant and product states with energies $\acute{\varepsilon}_{\mathrm{reactant}}$ and $\acute{\varepsilon}_{\mathrm{product}}$, respectively, such that the new reaction energy $\acute{\varepsilon}_r=\acute{\varepsilon}_{\mathrm{product}}-\acute{\varepsilon}_{\mathrm{reactant}}$ satisfies the conditions given in (i). In this case the local energy evaluation carried out will have to loop over another layer of particles within an interaction distance of the particles being rearranged.

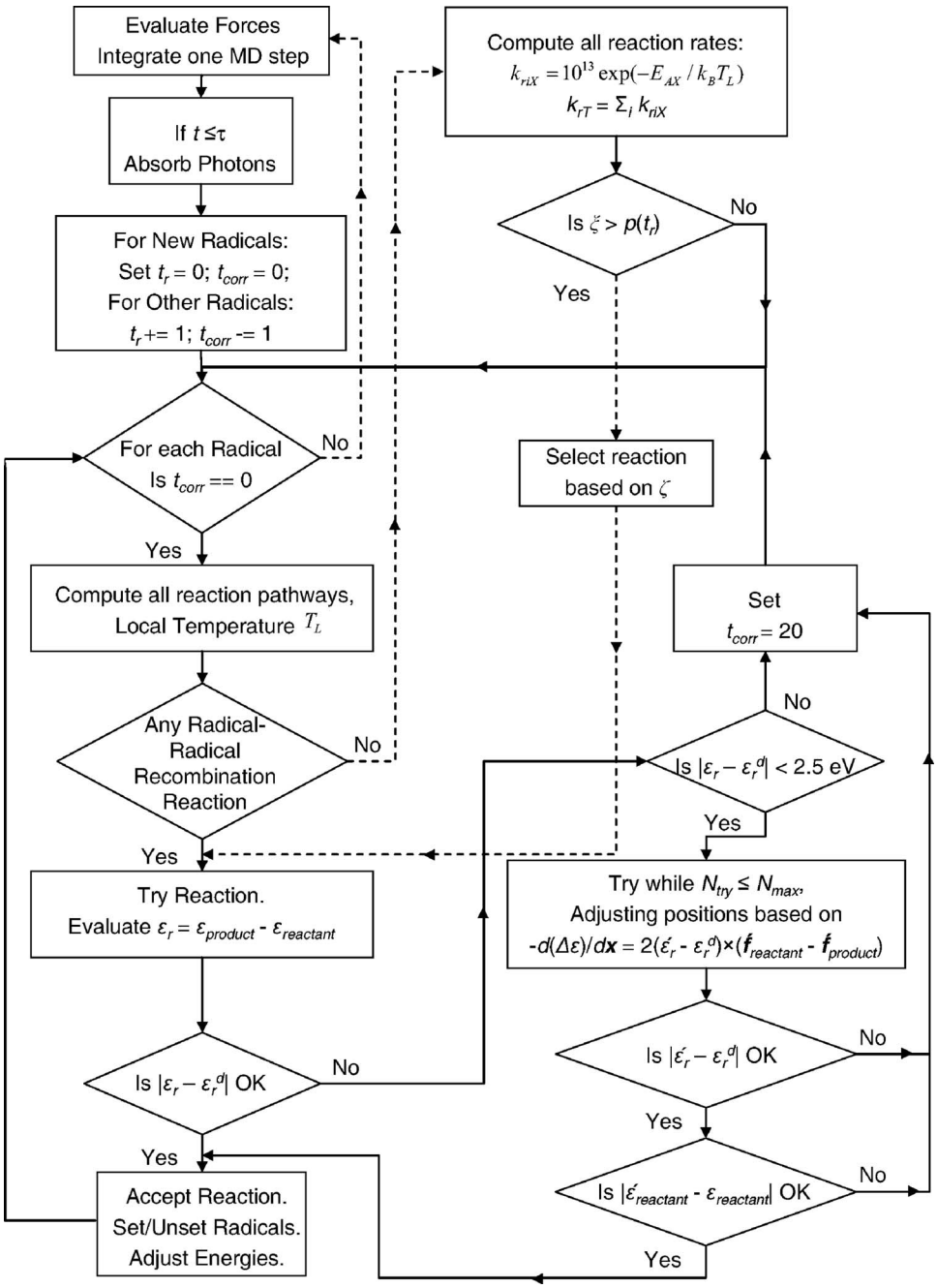

FIG. 5. The flow chart for the Monte Carlo chemical reaction scheme embedded within the MD time integration. Some flow lines are dashed for visual clarity.

- The optimization process minimizes the quadratic energy difference function given by $\Delta\varepsilon = (\acute{\varepsilon}_r - \varepsilon_r^d)^2$, by moving the particles based on the directions given by its derivative

$$d(\Delta\varepsilon)/d\boldsymbol{x} = 2(\acute{\varepsilon}_r - \varepsilon_r^d) \times (\acute{\boldsymbol{f}}_{\text{reactant}} - \acute{\boldsymbol{f}}_{\text{product}}), \tag{6}$$

  where $\boldsymbol{x}$ and $\acute{\boldsymbol{f}}$ represent the positions and forces of all the particles being moved.

- The optimized states $\acute{\varepsilon}_{\text{reactant}}$ and $\acute{\varepsilon}_{\text{product}}$ and consequently the reaction may be accepted if the total energy adjustment required which is the difference between the new and the original reactant state, $\acute{\varepsilon}_{\text{reactant}} - \varepsilon_{\text{reactant}}$, is not more than 5% of the thermal (kinetic) energy of the particles being rearranged.

- If the optimized states are rejected, or if the optimization fails to generate acceptable states satisfying condition set in (i) within $N_{\max} = 20$ steps, the substrate is restored back to its original MD state.

(f) If the reaction is accepted, the energy released (or required) is added to (or subtracted from) the kinetic energies of the reacting species to maintain energy conservation. Likewise, if the reaction was accepted based on the optimized states, the kinetic energy of all the particles being rearranged is scaled (by a ratio between 0.95 and 1.05) to conserve total energy. Upon acceptance, any existing radical tag among the reactants is removed and newly formed radicals are tagged.

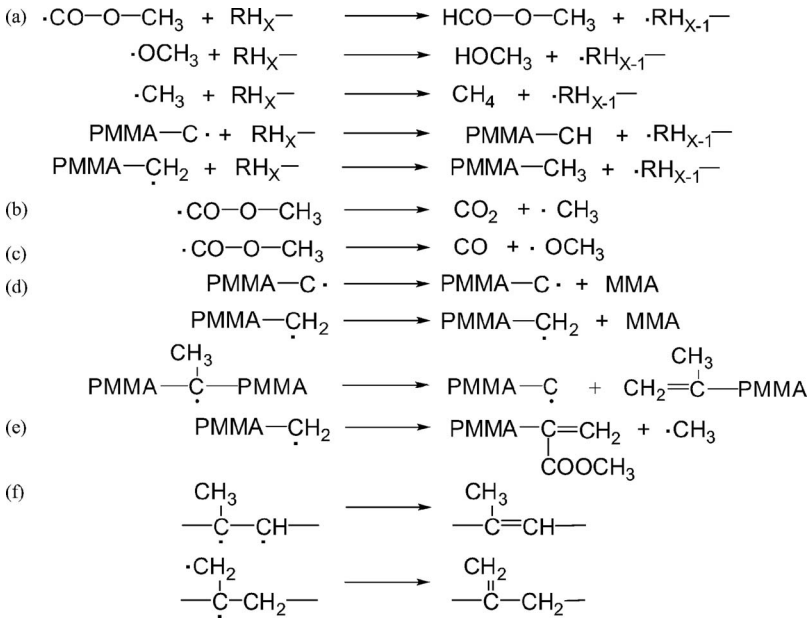

FIG. 6. The set of chemical reactions taking place in a PMMA substrate upon laser induced bond breaks. For simplicity, the complete bonding structure is not shown for some molecules.

The 2.5 eV energy criteria listed above serve as a crude upper bound to determine suitability of the reactant state for optimization, whereas the 5% kinetic energy adjustment criterion sets a firmer limit to the range of acceptable solutions. This measure introduces a physically realistic constraint when performing chemical reactions, not only ensuring that reactions occur only when conditions are appropriate but also advancing them in the right direction so that they may occur earlier if the conditions are nearly suitable. For the set of simulations reported here, the average amount of kinetic energy change per particle, resulting from adjusting the positions of the particles, is very small, of the order of 10^{-3} eV per successful optimization.

The optimization process is extremely fast as it involves evaluating energies and forces over a small subset of particles and uses a variable step size based on the magnitude of forces for fast convergence. But the optimization scheme also scales linearly with the number of radicals, so at a certain radical concentration, the total optimization cost per time step may rise above the cost of a single MD time step. This burden is further reduced by starting a countdown clock set at $t_{corr}=20-50$ MD time steps for every radical with failed reaction or optimization attempt. Thus, a reaction for a radical is retried only when t_{corr} is at zero. The clock time t_{corr} is counted down every MD step. The average radical survival time, for the simulations reported here, is approximately 1 ps because of the high temperatures prevailing in the substrate.

IV. PMMA REACTION MODEL AND SIMULATION RESULTS

A. Chemical reactions

In the case of a PMMA substrate, there are two photochemical reaction pathways where photon energy can be utilized to "directly" break two types of bonds. In the first case, the Norrish type I reaction (see Fig. 1), the C–CO bond on a PMMA side chain is broken. In the second case, the Norrish type II reaction, the $C-CH_2$ bond on a polymer's main chain is broken. The equilibrium bond strength in each case is 3.6 eV, so excess photon energy goes into kinetic energy of the beads involved in the bond cleavage. The choice of the set of chemical reactions is based on the ablation products experimentally observed and the likely chemical reaction pathways suggested in the literature.[2,4,6,7,9,11,18,29,30,69] Experimental studies have demonstrated the presence of small gaseous molecules such as CO, CO_2, CH_4, $HCOOCH_3$, and CH_3OH as well as MMA monomers and smaller polymer fragments in the ablation plume. The reason for differences in observed products remains unclear and may arise from limited set of experimentally observed species or real mechanistic differences resulting from various starting radicals formed under diverse experimental conditions and following different reaction paths. The key point of contention in PMMA ablation is (a) whether it involves predominantly thermal or chemical mechanisms and (b) if it is chemical, which one of the photolysis pathways is preferred.

The reactions included in the MD-MC scheme for PMMA substrate can be categorized into six major types and are listed in Fig. 6. They are as follows: (a) hydrogen abstractions which can be performed by every radical depending on availability of a hydrogen rich species nearby; (b) decarboxylation; (c) carbon monoxide elimination; (d) polymer main chain unzipping; resulting in smaller fragments and monomeric MMA units; (e) elimination of CH_3 radical followed by formation of a double bond; and (f) a double bond formation for any two adjacent carbon radicals already joined by a single bond. The possibility of substrate modification leading to an incubation-like effect, which may play an important role in achieving ablation at longer wavelengths,[4,7,9,25] is also included in our photochemical scenarios. The carbon beads at a broken main chain site can form C=C which can then absorb photons and convert it only to heat. For this effect, however, the laser pulse width would have to be long enough to allow for sufficient number of unzipping reactions to occur and double bonds to form.

TABLE I. Activation and formation energies for all chemical reactions occurring in a PMMA substrate (in eV).

Reaction type	Activation energy	Formation energy
[(a), (i)] Hydrogen abstraction (by $-CH_x^{\bullet}$ radical)	0.43	−0.19
[(a), (ii)] Hydrogen abstraction (by $-O^{\bullet}$ radical)	0.14	−0.78
(b) Decarboxylation	0.59	−0.90
(c) Carbon monoxide removal	0.97	0.75
(d) Unzipping	0.94	0.67
(e) $^{\bullet}CH_3$ radical removal	1.16	0.93
(f) C=C formation	0.00	−2.76

Electronic structure calculations were performed[52] to measure the activation and reaction energies for each of these reactions [except (f) and (a), (ii)]. The radical-radical recombination reaction listed in (f) above occurs without any activation energy barrier and reaction energy equal to difference between strengths of a double bond and a single bond. The CH_3OH reaction energies were taken from *ab initio* calculations reported in Ref. 71. The activation and reaction energies are given in Table I. The choice of chemical reactions and their influence on the substrate are subjected to more detailed investigations reported elsewhere.[72–74]

B. Simulation and analysis setup

All simulations reported here were performed using $\lambda = 157$ nm and $\lambda = 248$ nm laser wavelengths, with energies of 7.9 and 5.0 eV/photon, respectively. These two wavelengths are among the commonly used wavelengths in the experimental studies reported on PMMA substrate.[2,4,6–9,11,18,29,30,69] Irradiation was carried out over a single pulse of pulse width $\tau = 150$ ps. The fluence range investigated was 8–15 mJ/cm^2, which was set based on the choice of penetration depth, $1/\alpha = 100$ Å, and Beer's law profile in the substrate satisfying the criteria given in Sec. III A. The largest PMMA sample (c) with 109 365 beads in a system of size $51 \times 51 \times 258$ Å^3 was used for the simulation. The ranges of fluence and penetration depth are limited by the sample size and run time limitations inherent in any MD simulation.

The photon absorption process was set up such that all pathways are equally likely, i.e., 1/3 probability of each of pure heating, and Norrish type I and Norrish type II bond breaks. The purpose in doing so is to demonstrate the full range of physics that can be explored with our current modeling scheme. The simulations were monitored to ensure capture of all possible ablation, i.e., large cluster ejection, events. The total run times of simulations were in the range of 300–600 ps. The MD time integration was performed using Velocity-Verlet algorithm[75] with a step size of 1 fs. The total computational time for a single run of 500 000 time steps was about 2 weeks on a single processor.

The evaluation of substrate characteristics in terms of its density, temperature, pressure, chemical composition, and energy was done by dynamically slicing it into slabs, each of 10 Å thickness, along the direction of incident laser (z axis). During most of the simulation time frame, the spatial density profile shows a sharp transition separating the bulk substrate from the ejected plume. The yield was determined by summing up all the particles in the plume. The plume was further analyzed by identifying aggregates based only on their spatial separation. For this purpose, a cutoff distance of 5 Å was used to label interacting versus noninteracting beads as all the bonding potential energies go below the available thermal energy beyond a separation of 3.5–5 Å. The clusters are identified by grouping together all the ejected coarse grained beads found within a distance of 5 Å of each other. Average size was given by $S = M_2/M_1$, i.e., the ratio of second moment of cluster size distribution over its first moment.

C. Ablation yields

The primary observables in ablation studies, i.e., the yield and average size, appear to be a complex function of the fluence and the laser wavelength, as seen in their temporal evolution in Figs. 7(a)–7(d). The yields and average sizes differ for identical fluences at different wavelengths, both in terms of their evolution and their final values. An ablation threshold also appears to exist, demarcating desorption and ablation regimes, which can be identified in terms of the number and average sizes of the ejected clusters in Fig. 7. Below this threshold, e.g., for 8 mJ/cm^2 fluence with 157 nm laser, there is a smooth rise in the yield, with continuous ejection of smaller clusters ($S \sim 1$), consistent with the desorption regime. Above the threshold, many large cluster ejection events are observed during and after the irradiation time scale. The larger clusters, with average size $S \sim 1000$, appear to breakdown into smaller fragments over time. The exact value of the ablation threshold, however, appears to be a function of the laser wavelengths used, as we observe no ablation for 8 mJ/cm^2 fluence with $\lambda = 157$ nm laser, whereas 8 mJ/cm^2 fluence with $\lambda = 248$ nm laser does ablate. A detailed investigation into the ablation threshold as a function of laser processing parameters such as wavelength and pulse width will be reported in an upcoming publication.[74]

Selected snapshots from two different simulations—for (i) 8 mJ/cm^2 fluence at $\lambda = 157$ nm and (ii) 15 mJ/cm^2 fluence at $\lambda = 248$ nm—are shown in Fig. 8 corresponding to the end of the runs at 450 ps. These two runs show the opposite ends of the yield span, as seen in Fig. 7. The snapshots show the first run ejecting only small (MMA) monomer sized clusters while the second run ejecting large amount of gaseous particles (green colored beads in Fig. 8) and a few large clusters. In the first case, the laser irradiation results in swelling of the substrate, but it fails to eject any large chunks of material, whereas in the latter, there is substantially more swelling prior to ablation (not shown) followed by ejection

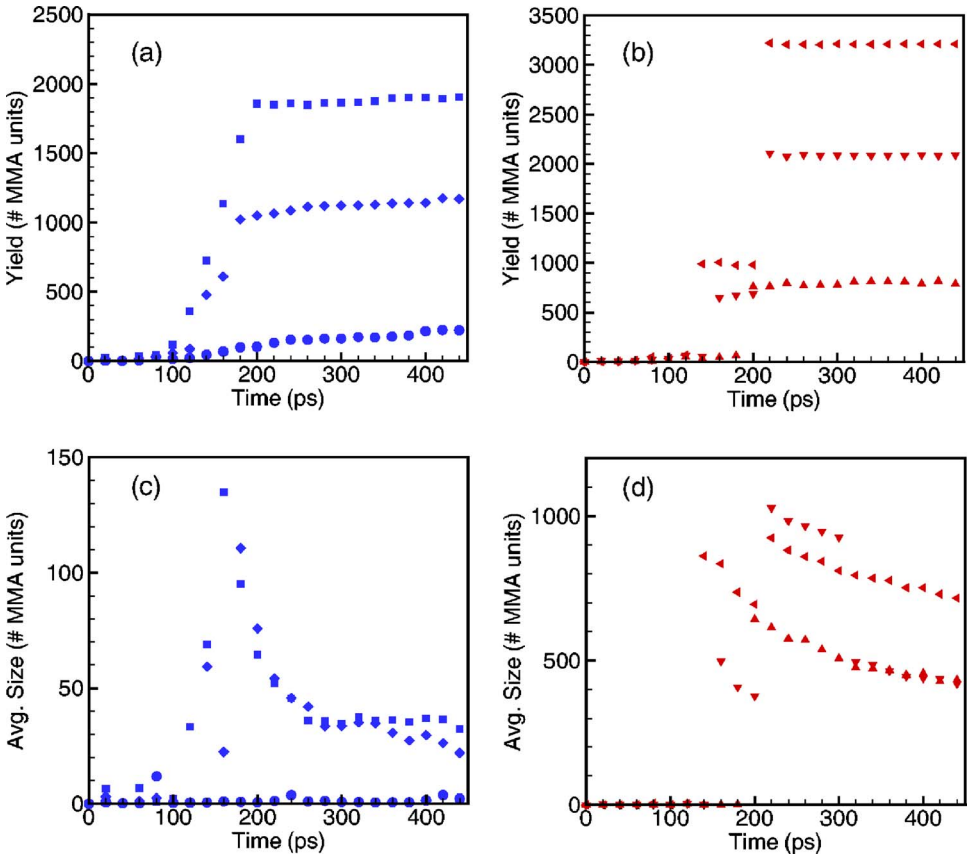

FIG. 7. (Color online) The evolution of yield, expressed in number of monomeric (MMA) units, as a function of time for (a) 157 nm simulations at 8 mJ/cm^2 (circles ●), 12 mJ/cm^2 (diamonds ♦), and 15 mJ/cm^2 (squares ■) fluences, and for (b) 248 nm simulations at 8 mJ/cm^2 (deltas ▲), 12 mJ/cm^2 (gradients ▼), and 15 mJ/cm^2 (left triangles ◀) fluences. The corresponding values of average sizes are given in (c) for 157 nm and in (d) 248 nm simulations, respectively.

of large amounts of gas molecules. This stage is followed later by ejection of the larger fragments and the gases trapped beneath them. The gas molecules also appear to be trapped within the larger clusters, which may be one of the reasons why these clusters fragment after ejection. Substrate modification, due to formation of radicals (yellow), gases (green), and double bonded polymer fragments and monomeric units (blue), up to the depth of 200–300 Å can be seen in Fig. 8 for both cases.

The ablation profiles can be understood by analyzing the processes taking place in the substrate following photon absorption. The absorbed photon can randomly perform substrate heating or one of Norrish type bond breaks. The energy involved in bond breaks and heating of the substrate is shown in Fig. 9, for 15 mJ/cm^2 fluence using $\lambda=248$ nm laser (i.e., the case corresponding to the highest yield). For this case, the laser is adding only about 163 eV/ps to the substrate, but the total energy added as heat is much greater, reaching up to 50% more than laser energy deposition rate. This excess energy is generated by numerous reactions among the photoradicals. The energy leftover following a bond break in Norrish type breaks also contributes to heating of the substrate. Only a small part of the laser energy is utilized for bond breaks, starting with about 50% of the laser energy and then settling down to 33% by 70 ps. This discrepancy is a consequence of the polymer unzipping reactions induced by main chain bond breaks (incubation like effect). These reactions lead to generation of unsaturated polymer fragments and monomers which prevent further photochemical scission and instead lead to deposition of energy as heat. As a result of this reaction only about 40%–45% of the photons are used for Norrish type bond scissions in all cases instead of the specified 67%. A more detailed study of the effect of this substrate modification will be reported elsewhere.[73,74] The energy generated by reactions continues to heat the substrate for a long time, but on a much smaller scale. Unzipping and hydrogen abstraction reactions will continue until all the radicals are exhausted (i.e., terminated

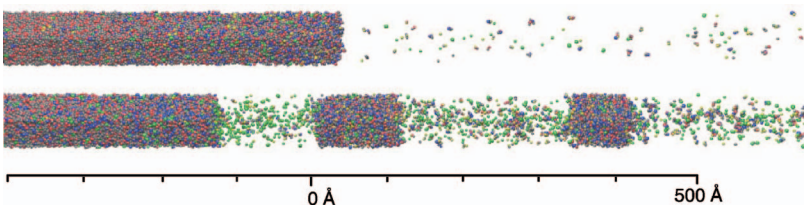

FIG. 8. (Color) The snapshots for two of the simulations: (top) $\lambda=157$ nm at 8 mJ/cm^2 fluence and (bottom) $\lambda=248$ nm at 15 mJ/cm^2 fluence. The depth scale (in Å) at zero represents the original top surface. The colors represent original polymer beads (gray), gaseous species (green), and doubly bonded carbon beads (blue). The red colored beads represent oxygen in the original and the transformed substrate.

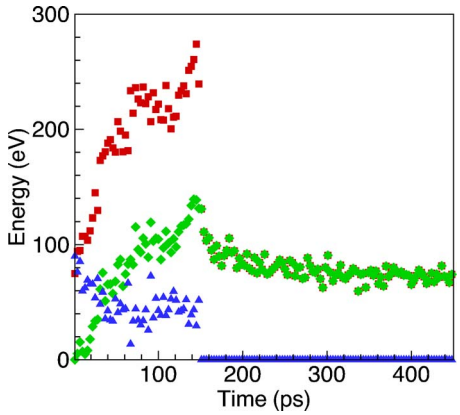

FIG. 9. (Color online) The distribution of energy (in eV) in the substrate, for $\lambda=248$ nm at 15 mJ/cm^2 fluence, as a function of time, in terms of energy consumed by bond breaks (triangles ▲), energy added as heat by reactions (diamonds ♦), and total energy added as heat by both laser irradiation and reactions (squares ■). The total energy and the energy added by reactions overlaps after the end of the laser pulse.

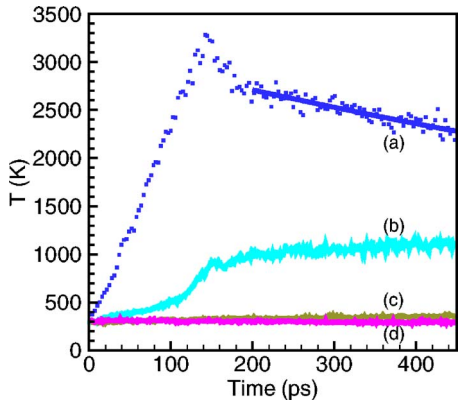

FIG. 11. (Color online) The kinetic temperature (in K), measured using lateral (xy) velocities, as a function of time. The values correspond to the depths of (a) 100 Å, (b) 300 Å, (c) 600 Å, and (d) 900 Å below the original surface, respectively. The line represents a least squares exponential fit to the temperature. The simulation parameters are the same as those given in Fig. 9.

or ejected) or the substrate cools down substantially. The role of photochemical processes in altering the spatial and temporal profiles of the laser energy deposition is similar to that reported earlier for organic solids.[47,49]

The thermal and chemical processes interact synergistically and play a crucial role in the transformation of the substrate. High temperatures lead to rapid reactions among the photoradicals which in turn lead to generation of more energy as heat, especially from creation of unsaturated carbon centers [reactions (d)–(f) in Fig. 6]. The generation of photoproducts occurs rapidly upon formation of radicals as shown in Fig. 10 for 15 mJ/cm^2 fluence using $\lambda=248$ nm laser. The small molecules such as CH_4 and CO_2 which arise out of exothermic decarboxylation of the cleaved PMMA side chain [reaction (b) in Fig. 6] appear immediately along with the double bonded carbon centers, C═, formed by exothermic unzipping and termination reactions. These are followed by endothermic reaction products such as CO and

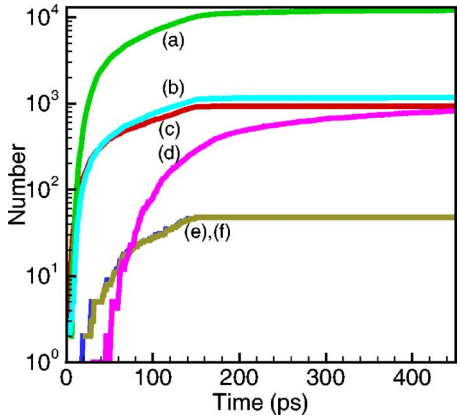

FIG. 10. (Color online) The total number of photoproducts and broken bonds produced in the sample as a function of time. The lines correspond to, from top to bottom, (a) the number of double bonded carbons, i.e, C═, (b) the number of molecules of CH_4, (c) the number of molecules of CO_2, (d) the total number of broken bonds, (e) the number of molecules of CO, and (f) the number of molecules of CH_3OH. The lines (e) and (f) are almost overlapping. The simulation parameters are the same as those given in Fig. 9.

CH_3OH [reaction (c) in Fig. 6]. The relative concentrations of these products are also much smaller than the products formed earlier. Early formation of these small gaseous photoproducts leads to their ejection from the substrate as seen in the snapshot in Fig. 8. The formation and ejection of these gases play a crucial role in the onset of ablation which will be investigated in detail later.[73,74] In contrast, the appearance of thermally and stress induced bond breaks occurs much later at around 45–50 ps. The photothermal bond break process is much slower owing to large covalent bonding energies as well as the intertwined nature of the polymer substrate. The photothermal process is also inefficient compared to the photochemical processes as it used up about 60% of laser energy and all the extra thermal energy generated by chemical reactions to achieve a relatively smaller level of fragmentation in the substrate. Figure 10 also demonstrates that most of the reactions take place during the time frame of laser irradiation and end with the laser pulse. Only unzipping and photothermal breaks continue to occur after the laser pulse is over.

The bulk of the laser energy is deposited in the top 100–300 Å of the substrate, due to the exponential profile of laser energy deposition, as can be seen in the temperature profiles in Fig. 11. The temperature at the depth of 100 Å reaches a maximum value of 3300 K at the end of the pulse. This is followed by a rapid drop due to material ejection and then a slower drop due to evaporation and conduction of heat to the cooler parts of the sample. At the depth of 300 Å the temperature rises only to about 1000–1100 K before leveling off over the MD time scale. Also as Fig. 11 shows, the temperatures at the depth of 600 Å and at the bottom of the sample (900 Å) barely rise above 300 K during the MD time scale. The highest temperatures observed in the substrate are artificially *inflated*, when compared to experimental values,[9,32,76] partly due to the MD simulation setup with reduced electronic and atomic degrees of freedom arising out of coarse graining of the polymer. These missing components result in a lower than realistic heat capacity and poorer conductivity. These approximations in the MD model may have adverse implications on the ablation dynamics, e.g.,

initiating rapid thermal decomposition of the polymer preventing a study of the role of photochemical bond breaks and chemical reactions.[13,15] However, in the case of our PMMA system we do not observe such an outcome. As seen in Fig. 10, the photothermal bond break process is much slower and the number of thermally unzipped or broken bonds is much smaller compared to the total number of photochemically generated species. Over longer time frame thermal decomposition of the polymeric substrate will dominate, especially after photoradicals are exhausted. The effect of high temperature on this slow decomposition process will be limited as the substrate is expected to cool rapidly. Based on the exponential fit shown in Fig. 11, the highest temperature will drop down to less than 1000 K in about 2 ns.

Pressure builds up in the substrate mainly due to the influence of thermal and chemical processes, namely, the substrate heating and the formation of gaseous photoproducts in a confined volume over a short period of time. This rise in pressure has been referred to as photothermal and photochemical pressure generation.[76] However, in order for the pressure to accumulate, inertial or stress confinement is required, which can be achieved within a characteristic stress confinement time given by, $t_{ac}=d/c$,[37] where d is the smallest dimension of the irradiated volume, corresponding to either the penetration depth or the laser spot size. For the penetration depth used here, this time works out to ~5 ps, i.e., much smaller than the 150 ps pulse used here. Consequently, high pressures and pressure gradients arising out of pressure waves are not observed in the simulations reported here. Further simulations at shorter pulse widths will look into the stress confinement regime and the role of photomechanical processes in ablation.[72–74]

V. CONCLUSIONS

In this article we have presented an enhanced version of the coarse grained chemical reaction model which integrates a Monte Carlo based chemical reaction scheme within a molecular dynamics simulation framework. This scheme can model the varied phenomena of thermal, mechanical, and chemical nature occurring during laser irradiation and ablation of polymeric materials. The model requires prior knowledge of the atomistic scale physics of the polymer, similar to that routinely employed in MD simulations of polymers. It also requires an understanding of chemical characteristics, especially chemical decomposition pathways, of the polymeric substrate which can be obtained from experimental studies as well as theoretical first principles based calculations. This information is used to determine all possible reaction pathways for radicals present in the system. The reactions are then performed, based on the radical survival times and relative reaction rates, if their energy landscapes are favorable. The modeling scheme described here captures all the necessary physics occurring at the atomistic scale during ablation processes and can be applied to the study of a wide range of polymeric substrates.

The sample set of results, for the PMMA polymer, discussed in this article reveal how different processes are borne out of different photon energy absorption pathways. The interaction of thermal, chemical, and mechanical processes during irradiation and ablation plays a crucial role in transforming the substrate and establishing yield characteristics. The coupling of these processes highlights the usefulness of a unified framework to look at all these processes. The individual contributions of different photoexcitation pathways to the ablation process, which is the primary issue of contention in understanding ablation in PMMA, are hard to ascertain from the set of runs reported here as they have a mixture of all these pathways. Future studies will focus on isolating individual pathways, using specific set of experimental and modeling parameters, to identify their characteristic signature in the substrate and yield and establish their role in initiating ablation. Further studies with multiple wavelengths, penetration depths, and pulse widths along with different mixtures of photochemical-photothermal scenarios will replicate more realistic laser processing conditions and provide a better mechanistic understanding of the ablation process.

This coupled MD-MC modeling scheme is universal in the manner in which it integrates chemical reactions into the MD framework. Such a scheme can be useful in probing complex and intertwined physical and chemical processes occurring in highly reactive single or multicomponent systems, high temperature processing of materials, and fast energy deposition processes such as laser ablation and sputtering.

ACKNOWLEDGMENTS

This work was supported by the National Science Foundation through the Information Technology Research Program, Grant No. 0426604. The computer support was provided by the Academic Services and Emerging Technologies at Penn State University.

[1] C. J. Kulik, Proc. of SPIE, **5339**, 35 (2004)
[2] R. Srinivasan, B. Braren, D. E. Seeger, and R. W. Dreyfus, Macromolecules **19**, 916 (1986).
[3] R. Srinivasan and B. Braren, Chem. Rev. (Washington, D.C.) **89**, 1303 (1989).
[4] S. Kuper and M. Stuke, Appl. Phys. A: Mater. Sci. Process. **49**, 211 (1989).
[5] S. Kuper, S. Modaressi, and M. Stuke, J. Phys. Chem. **94**, 7514 (1990).
[6] M. Tsunekawa, S. Nishio, and H. Sato, J. Appl. Phys. **76**, 5598 (1994).
[7] D. J. Krajnovich, J. Phys. Chem. A **101**, 2033 (1997).
[8] T. Lippert, A. Yabe, and A. Wokaun, Adv. Mater. (Weinheim, Ger.) **9**, 105 (1997); E. Rebollar, G. Bounos, M. Oujja, C. Domingo, S. Georgiou, and M. Castillejo, J. Phys. Chem. B **110**, 14215 (2006).
[9] T. Lippert, R. L. Webb, S. C. Langford, and J. T. Dickinson, J. Appl. Phys. **85**, 1838 (1999).
[10] H. Tamura, T. Kohama, K. Kondo, and M. Yoshida, J. Appl. Phys. **89**, 3520 (2001); T. Efthimiopoulos, C. Kiagias, G. Heliotis, and E. Helidonis, Can. J. Phys. **78**, 509 (2000).
[11] T. H. Fedynyshyn, R. R. Kunz, R. F. Sinta, R. B. Goodman, and S. P. Doran, J. Vac. Sci. Technol. B **18**, 3332 (2000).
[12] P. E. Dyer, Appl. Phys. A: Mater. Sci. Process. **77**, 167 (2003).
[13] T. Lippert and J. T. Dickinson, Chem. Rev. (Washington, D.C.) **103**, 453 (2003).
[14] T. Lippert, Plasma Processes Polym. **2**, 525 (2005).
[15] N. Bityurin, Annual Reports on the Progress of Chemistry, Section C (Physical Chemistry), **101**, 216 (2005).
[16] R. E. Johnson, in *Large Ions: Their Vaporization, Detection and Structural Analysis*, edited by T. Baer, C. Y. Ng, and I. Powis (Wiley, New York, 1996), p. 49; F. Hillenkamp and M. Karas, Int. J. Mass. Spectrom. **200**, 71 (2000); D. Bäuerle, *Laser Processing and Chemistry* (Springer-

Verlag, Berlin, 2000); N. H. Niemz, *Laser Tissue Interactions: Fundamentals and Applications*, 2nd ed. (Springer, Berlin, 2002); D. Gomez, I. Goenaga, I. Lizuain, and M. Ozaita, Opt. Eng. (Bellingham) **44**, 051105 (2005).
[17] A. Rohlfing, C. Menzel, L. M. Kukreja, F. Hillenkamp, and K. Dreisewerd, J. Phys. Chem. B **107**, 12275 (2003).
[18] A. Gupta, R. Liang, F. D. Tsay, and J. Moacanin, Macromolecules **13**, 1696 (1980).
[19] G. M. Davis and M. C. Gower, Appl. Phys. Lett. **50**, 1286 (1987); R. Srinivasan, B. Braren, and K. G. Caser, Pure Appl. Chem. **62**, 1581 (1990); D. Riedel and M. C. Castex, Appl. Phys. A: Mater. Sci. Process. **69**, 375 (1999).
[20] J. O. Choi, J. A. Moore, J. C. Corelli, J. P. Silverman, and H. Bakhru, J. Vac. Sci. Technol. B **6**, 2286 (1988).
[21] W. Xiaoning, A. T. William, and D. D. Dana, J. Chem. Phys. **99**, 4140 (1993).
[22] P. E. Dyer and R. Srinivasan, Appl. Phys. Lett. **48**, 445 (1986).
[23] E. H. David and D. D. Dana, Appl. Phys. Lett. **64**, 715 (1994); E. H. David, F. Jens, D. D. Dana, L. C. Eric, and J. F. James, Appl. Phys. Lett. **65**, 3051 (1994); E. H. David, F. Jens, and D. D. Dana, J. Appl. Phys. **77**, 5950 (1995).
[24] E. J. Harbron, V. P. McCaffrey, R. X. Xu, and M. D. E. Forbes, J. Am. Chem. Soc. **122**, 9182 (2000); C. Wochnowski, M. A. Shams Eldin, and S. Metev, Polym. Degrad. Stab. **89**, 252 (2005).
[25] G. B. Blanchet, P. Cotts, and C. R. Fincher, J. Appl. Phys. **88**, 2975 (2000).
[26] Y. Ito, J. Tadano, and M. Matsukura, Proc. of SPIE, 5662, 444 (2004).
[27] S. Kuper, J. Brannon, and K. Brannon, Appl. Phys. A: Mater. Sci. Process. **56**, 43 (1993); A. Costela, I. Garciamoreno, F. Florido, J. M. Figuera, R. Sastre, S. M. Hooker, J. S. Cashmore, and C. E. Webb, J. Appl. Phys. **77**, 2343 (1995); A. A. Serafetinides, M. I. Makropoulou, C. D. Skordoulis, and A. K. Kar, Appl. Surf. Sci. **180**, 42 (2001); M. Hauer, D. J. Funk, T. Lippert, and A. Wokaun, Opt. Lasers Eng. **43**, 545 (2005).
[28] B. Giannis, K. Andreas, S. Taxiarhos, V. Erene, and G. Savas, J. Appl. Phys. **98**, 084317 (2005).
[29] R. C. Estler and N. S. Nogar, Appl. Phys. Lett. **49**, 1175 (1986).
[30] B. Danielzik, N. Fabricius, M. Rowekamp, and D. v. d. Linde, Appl. Phys. Lett. **48**, 212 (1986).
[31] J. Kruger, S. Martin, H. Madebach, L. Urech, T. Lippert, A. Wokaun, and W. Kautek, Appl. Surf. Sci. **247**, 406 (2005); E. Rebollar, G. Bounos, M. Oujja, S. Georgiou, and M. Castillejo, J. Phys. Chem. B **110**, 16452 (2006); G. Bounos, A. Athanassiou, D. Anglos, and S. Georgiou, Chem. Phys. Lett. **418**, 317 (2006).
[32] B. Giannis, S. Alexandros, G. Savas, R. Esther, C. Marta, and B. Nikita, J. Appl. Phys. **100**, 114323 (2006).
[33] H. H. G. Jellinek and R. Srinivasan, J. Phys. Chem. **88**, 3048 (1984); V. Srinivasan, M. A. Smrtic, and S. V. Babu, J. Appl. Phys. **59**, 3861 (1986).
[34] E. Sutcliffe and R. Srinivasan, J. Appl. Phys. **60**, 3315 (1986).
[35] B. J. Palmer, T. Keyes, R. H. Clarke, and J. M. Isner, J. Phys. Chem. **93**, 7509 (1989); L. I. Kalontarov and R. Marupov, Chem. Phys. Lett. **196**, 15 (1992); S. R. Cain, J. Phys. Chem. **97**, 7572 (1993).
[36] N. Bityurin, B. S. Luk'yanchuk, M. H. Hong, and T. C. Chong, Chem. Rev. (Washington, D.C.) **103**, 519 (2003).
[37] G. Paltauf and P. E. Dyer, Chem. Rev. (Washington, D.C.) **103**, 487 (2003).
[38] A. Vogel and V. Venugopalan, Chem. Rev. (Washington, D.C.) **103**, 2079 (2003).
[39] B. Luk'yanchuk, N. Bityurin, M. Himmelbauer, and N. Arnold, Nucl. Instrum. Methods Phys. Res. B **122**, 347 (1997); N. Arnold, N. Bityurin, and D. Bauerle, Appl. Surf. Sci. **138–139**, 212 (1999).
[40] N. Bityurin, Appl. Surf. Sci. **138–139**, 354 (1999).
[41] H. Schmidt, J. Ihlemann, B. Wolff-Rottke, K. Luther, and J. Troe, J. Appl. Phys. **83**, 5458 (1998).
[42] B. J. Garrison and R. Srinivasan, Appl. Phys. Lett. **44**, 849 (1984).
[43] H. Kim and D. D. Dlott, J. Chem. Phys. **94**, 8203 (1991); H. J. Kim, D. D. Dlott, and Y. D. Won, *ibid.* **102**, 5480 (1995); H. J. Kim and Y. D. Won, J. Phys. Chem. **100**, 9495 (1996); L. Dutkiewicz, R. E. Johnson, A. Vertes, and R. Pedrys, J. Phys. Chem. A **103**, 2925 (1999).
[44] L. V. Zhigilei, P. B. S. Kodali, and B. J. Garrison, J. Phys. Chem. B **101**, 2028 (1997).
[45] L. V. Zhigilei, P. B. S. Kodali, and B. J. Garrison, J. Phys. Chem. B **102**, 2845 (1998); R. Knochenmuss and R. Zenobi, Chem. Rev. (Washington, D.C.) **103**, 441 (2003).
[46] L. V. Zhigilei and B. J. Garrison, Appl. Phys. A: Mater. Sci. Process. **69**, S75 (1999); L. V. Zhigilei and B. J. Garrison, J. Appl. Phys. **88**, 1281 (2000); L. V. Zhigilei, Y. G. Yingling, T. E. Itina, T. A. Schoolcraft, and B. J. Garrison, Int. J. Mass. Spectrom. **226**, 85 (2003).
[47] Y. G. Yingling, L. V. Zhigilei, and B. J. Garrison, J. Photochem. Photobiol., A **145**, 173 (2001).
[48] Y. G. Yingling, L. V. Zhigilei, and B. J. Garrison, Nucl. Instrum. Methods Phys. Res. B **180**, 171 (2001).
[49] Y. G. Yingling and B. J. Garrison, Chem. Phys. Lett. **364**, 237 (2002).
[50] K. O. Koji, H. Shinji, T. S. Phillip, M. Eizi, S. Volker, S. Kazuhiko, H. Yoshiya, and U. Nobuo, J. Appl. Phys. **83**, 4292 (1998); D. Troya and G. C. Schatz, Int. Rev. Phys. Chem. **23**, 341 (2004).
[51] S. I. Stoliarov, P. R. Westmoreland, M. R. Nyden, and G. P. Forney, Polymer **44**, 883 (2003).
[52] P. F. Conforti and B. J. Garrison, Chem. Phys. Lett. **406**, 294 (2005).
[53] Y. G. Yingling and B. J. Garrison, J. Phys. Chem. B **108**, 1815 (2004).
[54] Y. G. Yingling and B. J. Garrison, J. Phys. Chem. B **109**, 16482 (2005).
[55] D. Perez and L. J. Lewis, Phys. Rev. B **67**, 184102 (2003); L. Patrick, J. L. Laurent, and M. Michel, *ibid.* **73**, 134108 (2006); C. Changrui and X. Xianfan, *ibid.* **72**, 165415 (2005).
[56] W. K. Kim and L. M. Hayden, J. Chem. Phys. **111**, 5212 (1999).
[57] J. J. L. Cascales, F. G. Díaz, and J. G. de la Torre, Polymer **36**, 345 (1995).
[58] S. Wu, *Polymer Interface and Adhesion* (Dekker, New York, 1982).
[59] K. Ute, N. Miyatake, and K. Hatada, Polymer **36**, 1415 (1995); M. Tsige and P. L. Taylor, Phys. Rev. E **65**, 021805 (2002); A. Soldera, Polymer **43**, 4269 (2002).
[60] R. M. Sok, H. J. C. Berendsen, and W. F. v. Gunsteren, J. Chem. Phys. **96**, 4699 (1992).
[61] N. F. A. vanderVegt, W. J. Briels, M. Wessling, and H. Strathmann, J. Chem. Phys. **105**, 8849 (1996).
[62] S. B. Sane, T. Cagin, W. Knauss, and W. A. Goddard III, J. Comput.-Aided Mater. Des. **8**, 87 (2001).
[63] L. V. Zhigilei and B. J. Garrison, Mater. Res. Soc. Symp. Proc. **538**, 491 (1999).
[64] C. Schafer, H. M. Urbassek, L. V. Zhigilei, and B. J. Garrison, Comput. Mater. Sci. **24**, 421 (2002).
[65] R. W. Warfield, Die Makromolekulare Chemie **175**, 3285 (1974).
[66] G. C. John, J. Chem. Phys. **58**, 374 (1973); I. Gilmour, A. Trainor, and R. N. Haward, J. Polym. Sci., Part B: Polym. Phys. **16**, 1291 (1978).
[67] L. Yung-Chun, C. B. Kathleen, W. W. Frank, and S. Wolfgang, Appl. Phys. Lett. **69**, 1692 (1996); M. Ralph, J. Appl. Phys. **96**, 7696 (2004).
[68] P. C. Beard and T. N. Mills, Proc. SPIE **3916**, 100 (2000).
[69] P. E. Dyer and R. Srinivasan, J. Appl. Phys. **66**, 2608 (1989).
[70] C. C. Battaile, D. J. Srolovitz, and J. E. Butler, J. Appl. Phys. **82**, 6293 (1997).
[71] D. A. Good and J. S. Francisco, J. Phys. Chem. A **106**, 1733 (2002).
[72] M. Prasad, P. F. Conforti, B. J. Garrison, and Y. G. Yingling, Appl. Surf. Sci. **253**, 6382 (2007); P. F. Conforti, M. Prasad, and B. J. Garrison, Appl. Surf. Sci. **253**, 6386 (2007).
[73] M. Prasad, P. F. Conforti, and B. J. Garrison, J. Appl. Phys. **101**, 103113 (2007)
[74] P. F. Conforti, M. Prasad, and B. J. Garrison, J. Phys. Chem. C, in press.
[75] D. Frenkel and B. Smit, *Understanding Molecular Simulation: From Algorithms to Applications* (Academic, New York, 2002).
[76] D. E. Hare, J. Franken, and D. D. Dlott, J. Appl. Phys. **77**, 5950 (1995).